# Absorption experiments on x-ray-heated mid-$Z$ constrained samples

T. S. Perry, P. T. Springer, D. F. Fields, D. R. Bach, F. J. D. Serduke, C. A. Iglesias, F. J. Rogers, J. K. Nash, M. H. Chen, B. G. Wilson, W. H. Goldstein, B. Rozsynai, R. A. Ward, J. D. Kilkenny, R. Doyas, L. B. Da Silva, C. A. Back, and R. Cauble
*Lawrence Livermore National Laboratory, P.O. Box 808, Livermore, California 94550*

S. J. Davidson, J. M. Foster, and C. C. Smith
*Atomic Weapons Establishment, Aldermaston, Reading RG7-4PR, United Kingdom*

A. Bar-Shalom
*Soreq Nuclear Research Center, Yavne, 81800 Israel*

R. W. Lee
*Department of Physics, 366 Le Conte Hall, University of California at Berkeley, Berkeley, California 94720-7300*
(Received 18 March 1996; revised manuscript received 11 July 1996)

Results of a niobium absorption experiment are presented that represent a major step in the development of techniques necessary for the quantitative characterization of hot, dense matter. The general requirements for performing quantitative analyses of absorption spectra are discussed. Hydrodynamic simulations are used to illustrate the behavior of tamped x-ray-heated matter and to indicate potential two-dimensional problems inherent in the technique. The absorption spectrum of a low-$Z$ material, in this case aluminum, mixed with niobium provides a temperature diagnostic, which together with radiography as a density diagnostic fully characterizes the sample. A discussion is presented of opacity calculations and a comparison to the measurements is given that illustrates the need for experiments to provide a critical test of theory. The experimental technique is placed in context with a review of previous measurements using absorption spectroscopy to probe hot, dense matter. It is shown that the overall experimental concepts, although understood, were not always achieved in previous experiments. [S1063-651X(96)03111-X]

PACS number(s): 52.25.−b, 07.85.−m, 32.30.Rj, 32.60.+i

## I. INTRODUCTION

High-powered lasers can be used to irradiate high-$Z$ targets producing x-ray fluxes that can volumetrically heat materials to substantial temperatures. This x-ray flux produces a state of high-energy density matter that can be studied by the recently developed techniques of absorption spectroscopy to yield detailed information [1]. The theoretical and experimental investigation of the x-ray-absorption characteristics of these plasmas is an active field of research with applications in astrophysics, inertial fusion, and x-ray laser production [1–4].

The initial goal of such experiments was to develop techniques that could provide meaningful quantitative data on radiative and material properties. The results could then be employed to verify theoretical models or to obtain primary data where theoretical models are not at a sufficient level of sophistication. Over the past several years procedures to improve these experiments have been pursued. Improvements include the capability to quantify x-ray-absorption sources and the development of spectrometers that can simultaneously measure temporal, spatial, and spectral information from a hot dense source. Although achieving technological proficiency is necessary, it is not sufficient for a full analysis of the data. In addition, an experimental configuration must be implemented that adequately records the various contributions to the spectrum with enough ancillary information to permit quantitative analysis. Thus the target design and geometry play a central role in the experiment.

The study of plasma radiative properties requires the simultaneous measurements of the temperature, density, and absorption, or emission, spectrum. The lack of simultaneity has been a weakness of most absorption measurements. For example, some experiments have relied on hydrodynamics simulations to infer the plasma temperature and density, while others provide measurements of the temperature, density, and absorption spectrum, but on separate experiments. We report here the development of a technique that allows the simultaneous measurements of the temperature, density, and absorption spectrum. This is made possible by two significant modifications of previous experiments. First, the density is obtained by employing a second spectrometer to monitor the sample expansion. Second, a mixture of niobium and aluminum is used to determine the temperature from the absorption spectrum of aluminum, which occurs in a spectral region distinct from niobium. That is, we are employing the results of previous experiments where it was proven that the temperature can be determined with an error of less than 3% by using detailed spectroscopic models to reproduce the observed aluminum absorption spectrum [1]. It is obvious by looking at the numerous details of the transmission from a moderate-$Z$ element that only a high-precision, well-

 

constrained experiment can provide a method to differentiate among competing theories.

Given the number of attempts to perform experiments of this kind and the number of fields in which these data can be used, the evolution of these experiments is not of isolated importance. In fact, the current experimental construct can be used as a basis to review other experimental work in the field. These experiments fall into three categories. First are the methods using the point projection spectroscopy technique, which is also used in the present experiment [1,2]. This method makes possible the simultaneous measurement of the plasma conditions and the appropriate spectral information. Second are the experiments using streak cameras to measure the backlight spectrum attenuated by the sample [3]. This method provides both time and spectral resolution, but does not allow the spatial resolution necessary to obtain all the signals simultaneously. As a result, a series of separate experiments is necessary to obtain the data. Finally, there are experiments that use a large area backlight with two spectrometers: one to measure the backlight source and a second to measure the absorption. This method has no spatial information and the temporal information is derived from the finite duration of the backlight [4]. We note that other absorption experiments that use point projection spectroscopy for nonlocal thermodynamic equilibrium studies will not be reviewed as these are further complicated by the large spatial gradients and difficulties inherent in kinetics modeling [5].

The layout of the paper is as follows. In Sec. II a discussion is given of the experimental requirements for obtaining quantitative absorption data from well-characterized plasma samples. In Sec. III two-dimensional hydrodynamic simulations are presented to describe the time-dependent behavior of a sample that is volumetrically heated and tamped. The results of absorption measurement from a mixture of aluminum and niobium, obtained simultaneously with the temperature and density, are presented in Sec. IV. In Sec. V a comparison with calculations is shown where we illustrate that the effort to provide a benchmark allows one to select among various calculations that would otherwise be of equal merit. With the experimental requirements set out in Sec. II, the general behavior of the plasma defined by the hydrodynamics simulations in Sec. III, and the successful employment of these requirements in Secs. IV and V, we discuss in Sec. VI several previous experiments in light of the current work. Finally, a summary is given in Sec. VII.

## II. REQUIREMENTS FOR AN ABSORPTION EXPERIMENT

The constraints on a quantitative absorption experiment are threefold. First, one must have a setup that permits the absorption spectrum to be obtained from the data. Second, the experiment must incorporate characterization of the plasma, e.g., independent measurements of the plasma temperature and density. Third, the need for theoretical models should be minimized and those models that are needed must be independently verified. These points are covered in detail below.

### A. Measurement of the absorption spectrum

The first requirement for quantitative analysis of the experiments is the determination of the absorption spectra resulting from a characterized backlight. In particular, when absolute absorption is to be measured, the various sources of the intensity contributing to the film exposure must be recorded in a manner that allows their separation. The contributing sources are intrinsic film fog, instrumental fluorescence, and sources that are spectrally dispersed: the backlight and the sample emission. In addition, the efficiencies associated with the experimental measurement, such as reflectivities and filter transmissions, must be calibrated. Since absolute calibration is difficult, it is preferable to have all the information recorded on the *same* piece of film. In this manner variations in film, film development, grating or crystal response, and filters are minimized. An example is shown is Fig. 1, where point projection spectroscopy is used to record the various contributions on a single piece of film.

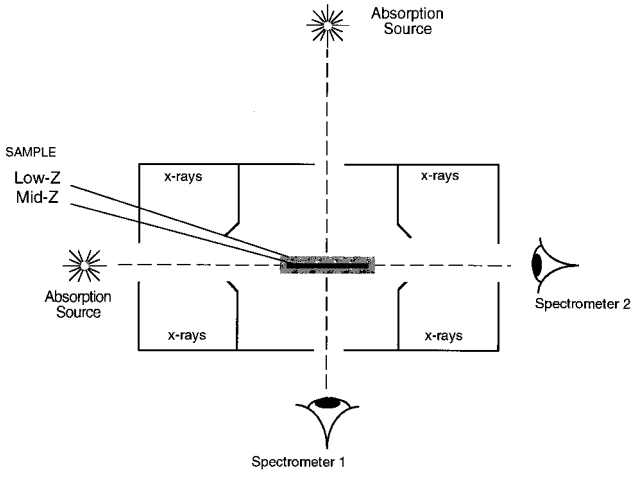


FIG. 1. (a) Schematic of an experiment designed to allow quantitative analysis of the absorption spectrum. The key elements are the backlight, the sandwich target, and a recording medium that allows the various sources to be measured at one time. (b) Schematic showing two spectrometers as used in the PPS technique.

The exposure, $E$ on film can be written as

$$E_{\text{film}} = E_{\text{fog}} + E_{\text{fluorescence}} + E_{\text{absorption}} + E_{\text{emission}}.$$

The inherent film fog must be subtracted from the data first. The remaining contributions are then converted from film exposure to intensity using calibrations provided, in the ideal case, by a step wedge being imposed on the original piece of film. This process produces the intensity information $I$, which can be written as

$$I_{\text{film}} = I_{\text{fluorescence}} + I_{\text{absorption}} + I_{\text{emission}},$$

which can be solved for the absorption spectrum

$$I_{\text{absorption}} = I_{\text{film}} - I_{\text{fluorescence}} - I_{\text{emission}}. \tag{1}$$

The frequency-dependent transmission through the sample $T(\nu)$ is given by

$$T(\nu) = \frac{I_{\text{absorption}}}{I_0} = e^{-\tau(\nu)}, \tag{2}$$

where $\tau$ is the optical depth of the sample and $I_0$ is the backlight source intensity. Thus, to obtain the frequency-

dependent information on the absorption, $I_0$ must be determined independently. Consequently, the same reduction used to obtain $I_{\text{absorption}}$ in Eq. (1) would be necessary to obtain $I_0$. The data analysis inherent in Eq. (1) is only correct if the emission sources are negligible or if the emission can be separated from the absorption.

If these conditions are met and the data are reduced consistently with Eqs. (1) and (2), then we could obtain the population densities, that is,

$$\tau(\nu)=\int \chi(\nu,l)dl, \tag{3}$$

where $\chi(\nu,l)$ is the frequency- and position-dependent absorption coefficient [6] and the integration is along the optical path. For a uniform sample

$$\tau(\nu)=\chi(\nu)L, \tag{4}$$

where $L$ is the total sample thickness. In turn,

$$\chi(\nu)=\sum_j n_j\alpha_j(\nu), \tag{5}$$

where $n_j$ and $\alpha_j(\nu)$ are the population- and frequency-dependent absorption cross section of state $j$. Using Eqs. (3)–(5), it is possible to obtain information on the plasma state by reduction of appropriately designed experiments.

Note that in the presence of gradients in the sample implies a loss of information since the populations are strongly dependent on plasma conditions. To minimize gradients one requires hydrodynamic isolation and expansion constraints on the sample. Isolation is essential, as shocks arising from material impinging on the target and any subsequent extraneous emission will confound the data interpretation. The constraints on the sample expansion assist in making the sample as uniform as possible, permitting, if uniformity is attained, the simplification inherent in Eq. (4).

The present experiments consider thin samples of moderate-$Z$ materials tamped, or constrained, by layers of lower-$Z$ elements. This allows the higher-$Z$ material to be volumetrically heated by an x-ray flux yet temporarily contained by the lower-temperature tamper. The result is a target heated throughout so that no shocks are driven into the sample; thus the sample remains relatively uniform.

This indicates that to obtain information on the absorption of the moderate-$Z$ sample one needs to measure the emission and absorption of the tamper and the emission of the full target. With recourse to Eqs. (1)–(3), assuming that fog and fluorescence levels can be obtained from the film data, we have

$$I_{\text{film}'}^{\text{CH}+Z}=I_{\text{emission}}^{\text{CH}+Z}+I_0^{\text{CH}+Z}e^{-\tau_{\text{CH}+Z}} \tag{6}$$

and

$$I_{\text{film}'}^{\text{CH}}=I_{\text{emission}}^{\text{CH}}+I_0^{\text{CH}}e^{-\tau_{\text{CH}}}, \tag{7}$$

where the subscript film′ indicates the signal measured after the fluorescence and fog has been removed. The superscript CH refers to the plastic tamper used in the present experiments, while $Z$ refers to the moderate-$Z$ sample. Solving for the transmission, we find

$$T^Z=\left(\frac{I_0^{\text{CH}}}{I_0^{\text{CH}+Z}}\right)\left(\frac{I_{\text{film}'}^{\text{CH}+Z}-I_{\text{emission}}^{\text{CH}+Z}}{I_{\text{film}'}^{\text{CH}}-I_{\text{emission}}^{\text{CH}}}\right). \tag{8}$$

Thus a transmission measurement requires six separate pieces of information, the emission, absorption, and backlight intensity of the CH and CH+Z. If we can ensure that the backlight is the same for both absorption measurements, the number of measurements is reduced to four:

$$T^Z=\left(\frac{I_{\text{film}}^{\text{CH}+Z}-I_{\text{emission}}^{\text{CH}+Z}}{I_{\text{film}'}^{\text{CH}}-I_{\text{emission}}^{\text{CH}}}\right). \tag{8}$$

Consequently, we could extract further information from the absorption coefficient, e.g., level populations, under the additional assumption of a uniform sample. If the material is not uniform, then we require information on the temperature and density variation to unfold the integral as indicated in Eq. (3).

### B. Independent characterization of the plasma

Equation (8) incorporates only the first condition necessary for quantitative results. The second condition is an independent characterization of the matter in which the absorption occurs. To use the absorption spectrum under investigation itself as a diagnostic would be circular; the characterization must be independent and verifiable.

In the current experiment we are interested in providing benchmark data for local thermodynamic equilibrium (LTE) opacity codes for a moderate-$Z$ element, niobium. We require, in addition to the absorption spectrum, four pieces of information on the sample itself: (i) the temperature, (ii) the density, (iii) the sample uniformity, and (iv) the degree of deviation from LTE. The sample uniformity and deviation from the LTE state have been addressed previously [1]. We have improved on past experiments by making temperature and density measurements simultaneous with the absorption measurement. The density measurement is performed with side-on imaging of the sample expansion, while the temperature is inferred from the absorption of the $K$-shell aluminum comixed with the niobium; see Fig. 1. The temperature measurement requires a theoretical model to derive a fundamental character of the sample from the observable, i.e., the spectrum. The independent verification of the model is the third and final requirement.

### C. Independent verification of models

The need to verify the models used to characterize the plasma implies that supporting experiments must be performed. In the present case we have verified that inferring the temperature from the absorption of the aluminum spectrum is accurate to a few percent [1]. This error in temperature includes a 20% error in the density measurement. To infer the density requires a reasonable estimate of the absorption oscillator strength and a measure of the length of the sample.

Note that the procedure does not depend on hydrodynamic simulations. All the plasma parameters are measured or inferred from previously verified mappings from observables to plasma parameters. It must emphasized that the use of hydrodynamic simulations is central to designing and understanding the performance of these volumetrically heated samples; however, we do not invoke the simulations as a diagnostic of the sample. Consequently, the design of the experiment hinges on the hydrodynamics, but this does not replace *in situ* diagnostic procedures.

## III. SIMULATIONS OF A SCHEMATIC EXPERIMENT

We now consider the heated sample in more detail and address questions concerning the analysis of the data using the plan laid out above. The primary questions are what the expected behavior of the sample is and what factors in the experiment will affect the evolution of the sample. The answers to these questions determine the range of validity for the analysis. The hydrodynamics simulations illustrate why x-ray-heated tamped targets are so advantageous for absorption experiments [1–4]. Briefly, these advantages are the following, (i) The use of a separable independent x-ray source to heat the sample allows the heating of the solid target by the x rays without the development of any hydrodynamic interaction between the heating source and the sample. (ii) Using x rays as the heating source avoids complex laser-matter interactions. (iii) The separability of the heating source and the sample permit an independent evaluation of the x-ray flux in isolation; thus one can use a source that is calibrated in time, angle, and frequency. (iv) The sample is confined on either side by a lower-$Z$ material creating a more homogeneous medium. Thus the design of the target controls the dimensionality of the experiment.

As commented above, the separation of the x-ray-heating source allows one to use a previously measured source as input to a hydrodynamic simulation. For example, the separation of the x-ray source can be achieved by using the x rays emitted from the rear side of a thin Au gold foil that has been well characterized [7]. The measured flux circumvents one of the uncertainties in the simulation of the target, i.e., simulations to derive the x-ray flux.

The known flux, together with a view factor calculation, was used in the simulation. The geometry of the simulated experiment is sketched in Fig. 2. For simplicity, the target was modeled as a disk. The x-ray source impinges along the $z$ direction and irradiates the sample equally from both sides of the $r$ axis. In the experiment, spectroscopy was performed through the sample in the $z$ direction and the radiography along the $r$ direction. Because of the twofold symmetry (about the $z$ and $r$ axes) the simulation is performed on one quadrant of the sample. The simulated target consists of two 1500-Å-thick layers of CH placed on either side of a medium-$Z$ element layer, here 3400 Å thick. CH was also placed on the ends of the sample (in the $r$ direction in Fig. 2). This target design, which we will refer to as fully tamped, is shown in Fig. 3(a), as well as on an identical sample without the end-tamping CH. This target is shown in Fig. 3(b). This geometry and these assumptions are consistent with the experiment discussed in Sec. IV. The radiation-hydrodynamics code LASNEX [8] was used with the measured x-ray source,

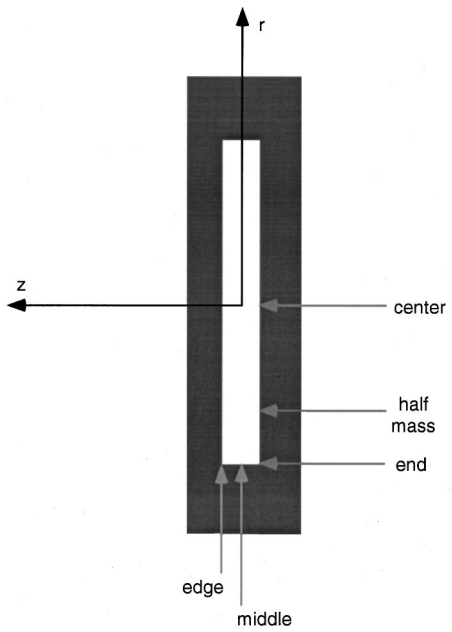


FIG. 2. Target geometry used in the simulation and a definition of the positions referred to in the text.

which had a duration of 1.1 ns. We note that due to the actual size of a holhraum target, which is a gold cylinder 0.75 cm long with a 0.5 cm diameter containing baffles to isolate the tamped sample from the laser-produced plasmas (see Fig. 1), the hydrodynamic isolation of the sample lasts for the first ~4 ns.

### A. Predicted conditions in a medium-$Z$ tamped sample

Although the simulations were performed in two dimensions it was found that one-dimensional (1D) simulations are

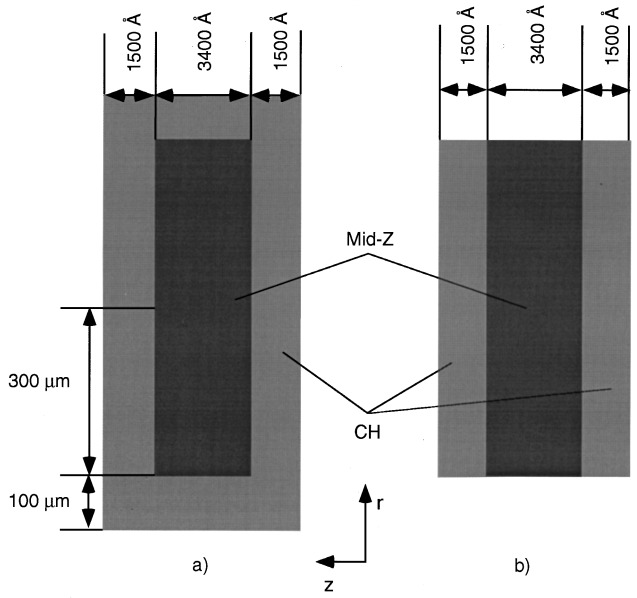


FIG. 3. Different target designs for two-dimensional hydrodynamics calculations. Note that both axes represent distance but with the abscissa in angstroms and the ordinate in micrometers. (a) The design completely imbedded in CH is an optimum design for minimizing lateral motion, while the design in (b) has no CH tamping at the ends.

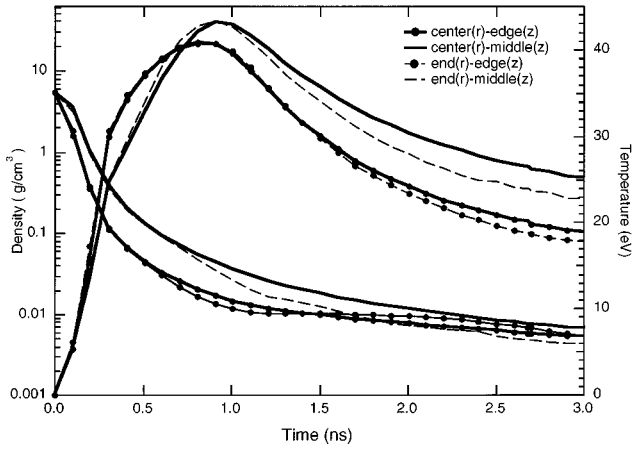


FIG. 4. Results for the heating of the mid-$Z$ sample for four positions in the sample as a function of time. The solid lines are along the center of the target, showing the middle and edge of the sample. The dashed lines show the end of the sample at the middle and edge. See Fig. 2 for a definition of the positions. The solid lines represent the sample center and the dashed lines represent the sample end.

adequate for the bulk of a *fully tamped* sample. In addition, LTE and non-LTE simulations predicted insignificant differences.

Figure 4 shows the evolution of the mid-$Z$ density and electron temperature at four points in the fully tamped sample. Referring to Fig. 2, the four points are center ($r$)-middle ($z$), center ($r$)-edge ($z$), end ($r$)-middle ($z$), and end ($r$)-edge ($z$). The two points along the center of the sample show gradients of density and temperature along the direction of the x-ray-absorption measurement, i.e., along the $z$ direction. The plots show that the temperature rises to a maximum of 40 eV at the peak of the heating pulse near 1 ns and that the absorption is nearly constant through the sample. Therefore there are only small ($<20\%$) temperature gradients in the sample at any time in the $z$ direction. As the sample expands a density gradient is created in the $z$ direction. Near 1 ns, the difference in density between the inner [middle ($z$)] and the outer [edge ($z$)] is about a factor of 2. As the heating pulse turns off the inner region is at a higher pressure than the edge and the relative faster expansion of the inner region reduces the density gradient.

The dashed lines in Fig. 4 are analogous to the solid lines, but at the end ($r$) of the sample, not in the center ($r$). The resulting values and gradients at the end ($r$) are very similar to results in the center ($r$). This indicates that throughout the simulation, conditions are not significantly different in the $r$ direction of a fully tamped sample. This will be discussed below.

### B. Importance of sample tamping

Ideally transmission experiments should have material undergo little change over the course of the measurement. Expansion of the sample in the direction perpendicular to the line of sight can affect conditions in the material. As shown below, this problem cannot be completely overcome by making a sample with a large initial aspect ratio ($r$ dimension to $z$ dimension) and restricting the region probed to the center of the sample.

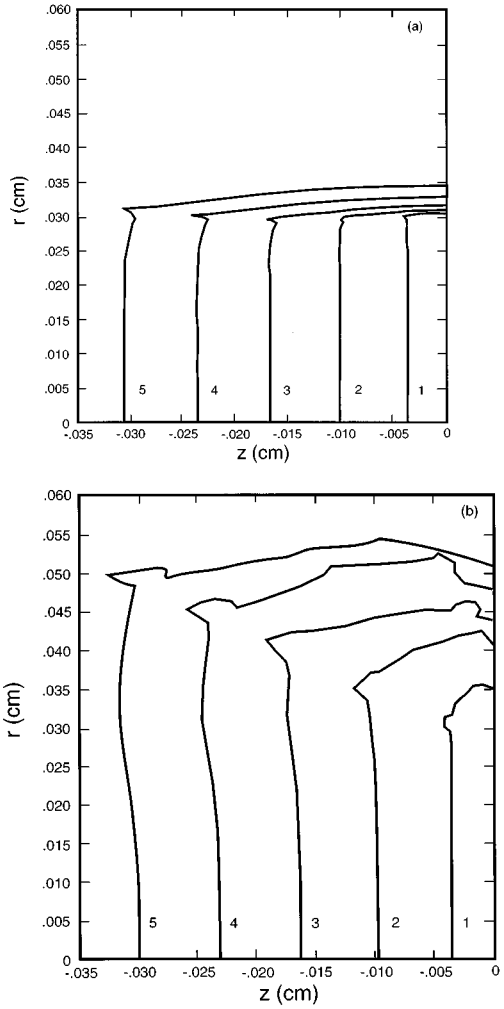


FIG. 5. Two-dimensional plot of $z$ versus $r$ for the end and edge at times 1–5 ns in the evolution of the sample. (a) Results for the fully tamped sample [Fig. 3(a)]. Each contour is labeled with the time in nanoseconds from the initiation of the x-ray pulse. (b) Same as (a) but for the partially tamped sample [Fig. 3(b)].

The behavior of tamped and untamped samples can be explored by simulating the two targets shown in Fig. 3. Figure 5 displays the predicted boundaries of the mid-$Z$ sample for these two target configurations. The numbers on the figure correspond to the number of nanoseconds into the simulation, where zero is the beginning of the x-ray heating pulse. The time duration for hydrodynamic isolation for the represent target would be $\sim$4 ns; however, we show results up to 5 ns to provide information for future experimental configurations. The $z$ positions of the sample edge ($z$) for the two cases near the center ($r$) of the sample ($r=0$) are nearly identical and are well represented by 1D simulations. However, there is a considerable difference near the sample end ($r$). The original end of the sample was at $r=0.03$ cm. In the fully tamped case [Fig. 5(a)] perpendicular expansion of the end is limited to 0.005 cm after 5 ns. In the untamped case [Fig. 5(b)], material has moved laterally nearly 0.025 cm by 5 ns, nearly doubling the $r$ dimension of the sample. This appears dramatic, but we need to determine if this perpendicular expansion affects the results of the absorption measurement.

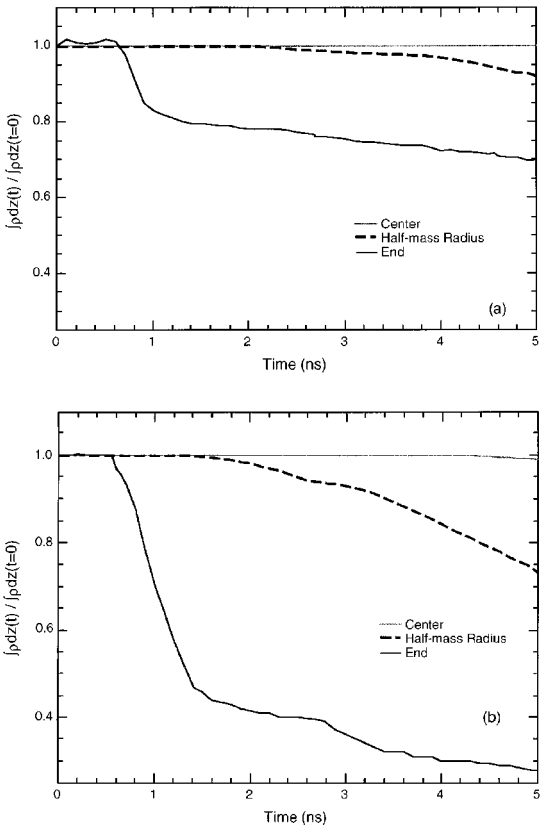


FIG. 6. Integral of density along the $z$ axis for three radial positions versus time. See Fig. 2 for definitions of the coordinate system. The integral along the $z$ direction at the center is represented by a solid line, the half-mass radius by a dotted line, and the end radius by a dashed line. (a) The fully tamped sample and (b) the partially tamped sample.

As indicated in Eqs. (2)–(5), the areal density $\rho z$, that is, the mass density $\rho$ integrated along the line of sight through the sample, is an essential ingredient in the analysis of the experiment. Figure 6(a) consists of time histories of $\rho z$ for the fully tamped sample at three different $r$ positions normalized to time zero,

$$\rho z(r,t)=\int_{r=\text{const}} dz\ \rho(z,t) \Big/ \int dz\ \rho(z,0).$$

The three positions are center ($r=0$), half-mass (the radius that contains half of the sample mass $r=0.0212$ cm), and the end ($r=0.03$ cm). A reduction in $\rho z$ from a value of one indicates that lateral expansion has reduced the material in the line of sight at that $r$ position. Clearly, the center ($r=0$) is unaffected up to 5 ns after the start of the heating pulse in the fully tamped sample. The half-mass point ratio shows some deviation after 2 ns, further decreasing to about 0.92 at 5 ns. The end ($r$) shows the most significant variation where $\rho z$ increases slightly at early times, caused by a small shock driven into the sample as the end attempts to expand against the inertia of the CH side tamper. Closer inspection indicates that the sample continues to decompress, with a roughly linearly velocity, so that the shock effect is localized. This small shock effect can be alleviated by better matching of the densities of the sample and tamper, but is

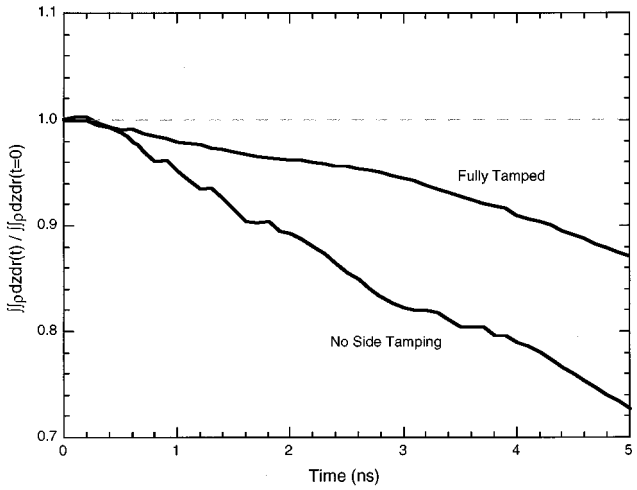


FIG. 7. Mean density averaged over the initial radius $\overline{\rho z}$ versus time fo the fully tamped sample (solid line) and the partially tamped sample (dot-dashed line). The short dashed line indicates $\overline{\rho z}=1$.

immaterial. The end ($r$) then quickly expands, reducing $\rho z$ to about 30% by $t=5$ ns. Figure 6(b) provides the same information for the sample without end tamping. In contrast with the fully tamped simulation, $\rho z$ exhibits more dramatic decreases, for example, by 5 ns, $\rho z$ at the half-mass radius has decreased by 25%, and at the untamped end it has decayed by more than 70%.

If the absorption is measured without spatial discrimination along the $r$ axis, then all the densities along the radius are sampled. In Fig. 7 the time behavior of the radially averaged $\overline{\rho z}$ defined by

$$\overline{\rho z(t)}=\int\int dr\ dz\ \rho(z,t) \Big/ \int\int dr\ dz\ \rho(z,0)$$

is displayed. The $r$ integration has been carried out to the original radius $r=0.3$ cm. At 5 ns, $\overline{\rho z}$ probed by an absorption source without spatial resolution drops to about 0.9 and 0.75 for a tamped and an untamped sample, respectively. Consequently, if the field of view can be limited and the sample completely constrained, then considerable confidence in the sample conditions can be obtained over the course of a measurement. However, the measurement of transmission without spatial discrimination, or with spatial discrimination but with a convolution of space and spectrum in one direction as in the point projection technique employed in Sec. IV, may provide data that are not at a single temperature and density.

## IV. ABSORPTION EXPERIMENT OF AN ALUMINUM-NIOBIUM MIXTURE

In the present experiment the temperature, density, and transmission of a plasma containing a mixture of niobium and aluminum was obtained. The simultaneous measurement required two changes from the earlier techniques [1]. To determine the density, a second point projection spectrometer was introduced to measure the sample expansion. The temperature was determined from the aluminum transmission spectrum. Aluminum as the temperature monitor has been

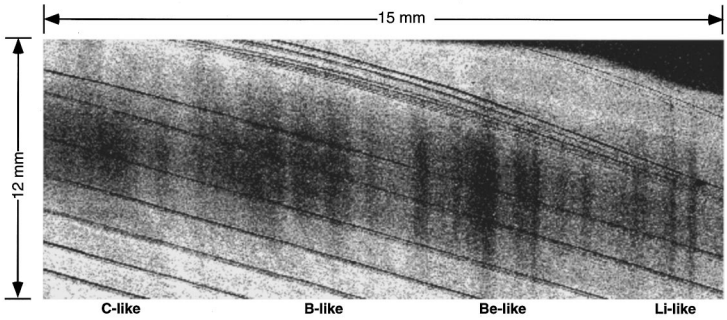


FIG. 8. Film data from spectrometer 2 used to measure the expansion of the sample. The spectral lines are aluminum absorption lines. The diagonal lines were caused by defects in the PET crystal and were numerically filtered out during the analysis.

verified as an accurate temperature diagnostic [1] and conveniently the absorption features of the aluminum and niobium lie in different parts of the spectrum.

The experimental arrangement is shown in Fig. 1. The basic technique is the method of point projection spectrometry (PPS) [9]. In this technique a point source of x rays is produced by tightly focusing a laser beam on a small, i.e., less than 100 $\mu$m, backlight fiber. X rays from the backlight pass through the sample onto an x-ray-diffraction crystal and are then recorded on film, as $I_{\rm film}^{\rm CH+Z}$ of Eq. (6). Other x rays from the same point backlight bypass the sample, but are also diffracted from the crystal, and used as $I_{\rm film}^{\rm CH}$ of Eq. (7). The ratio of the x-ray spectrum attenuated by the sample to the unattenuated x-ray spectrum provides the basic information as transmission $T^Z$ of Eq. (9). Moreover, the film fog and emission levels can be ascertained from the film record, so that all the contributions necessary to obtain $I_{\rm film}^{\rm CH+Z}$ are available; see Eq. (1).

The use of two point projection spectrometers and multiple crystals allows considerable flexibility. The first spectrometer, denoted as spectrometer 1 in Fig. 1, has two crystals and obtains the absorption spectrum from both the aluminum and the niobium. The thickness of the sample was chosen so that the strongest lines in the spectral range of interest have optical depths of order unity avoiding loss of information on the film record. The accuracy of the information obtained from absorption spectra with optical depth much larger than unity is compromised by extraneous background signal together with the finite instrument response and resolution.

The primary function of the second spectrometer, which is denoted as spectrometer 2 in Fig. 1, was to radiograph the sample as it expands. The accuracy of this measurement is limited by the assumed unidimensionality of the expansion and the contrast of the tamper and tamped material. The length of the sample was chosen so that the strongest lines were optically thick in this direction. This provided high contrast and allowed the width and thus the density of the sample to be accurately measured. As an additional benefit, in spectral regions where the optical depth is low, spectrometer 2 gave a more accurate value of the absorption.

In particular, the sample for the experiment was a thin foil of Nb mixed with Al and tamped by CH. The initial areal density of the sample was measured to 5% by x-ray fluorescence to be 222 $\mu$g/cm$^2$ of Nb and 35 $\mu$m/cm$^2$ of Al. Assuming that the Al and Nb were at nominal densities, this initial thickness would be 3940 Å, providing much smaller spatial gradients than the simulation results in Sec. III. In fact, simulation of this configuration leads to temperature gradient of less than 1% for all times of interest. The sample was made by a simultaneous evaporation of the Al and Nb onto CH and then overcoating with CH so that both sides of the sample were tamped. The sample was heated by x rays from a gold hohlraum target irradiated by $3\omega_0$ (0.35 $\mu$m wavelength) light from eight of the beams of the Nova laser. These beams had a total of 15 kJ of $3\omega_0$ light in a 1-ns square pulse. The backlight fibers, schematically shown in Fig. 1, were each irradiated by one $2\omega_0$ beam having 500 J in a 200-ps Gaussian pulse. The two beams used for the backlight were delayed by 2 ns after the eight-beam heating pulse. The simultaneity of the two backlights was measured to be 30 ps.

The data obtained from the spectrometers are shown in Figs. 8 and 9. Backgrounds were subtracted, as indicated in Eq. (1), and the film density was converted to intensity using the measured x-ray response of the Kodak type-C x-ray film. From spectrometer 2 the width measured from the Al 1–2 absorption features was $4.8\pm0.4$ mm, which agreed with the used of the continuum to obtain the width. The magnification of spectrometer 2 was 36, indicating a size of $133\pm11$ $\mu$m. Incorporating the size of the backlighter ($25\pm15$ $\mu$m) and the sample tilt ($8\pm1$ $\mu$m) gave the sample size of $100\pm19$ $\mu$m. Given the initial sample areal density and propagating errors yields a $26\pm5$ mg/cm$^3$ sample density at the time of interest. Note that the final measured density does not depend on any assumption about the density at which the Al and Nb were deposited. In Fig. 9 the film record from spectrometer 1 is presented. The spectrometer contained two penta-erythritol tetrakis (hydroxymethyl)-methane $C(CH_2OH)_4$ (PET) crystals. One of the crystals was oriented to measure the aluminum absorption spectrum between 1500 and 1600 eV. The other crystal was oriented to measure the niobium absorption spectrum between 2000 and 3000 eV. To calibrate the spectral energy on the Nb spectrum Zr and Mo $L$ edges were used.

Figure 10 shows the reduced Al spectrum, which shows contributions from Li-like to C-like ions. Using the OPAL opacity code [10], which calculates the spectrum using a detailed transition accounting scheme modified to have spectroscopically accurate energy levels [11], a best fit was obtained with the experimental spectrum to determine the temperature using the measured density. The OPAL calculations included a 0.7 eV instrumental resolution. This fit is also shown in Fig. 10. The theoretical spectrum is sensitive to small changes in temperature, but is a weak function density, providing the link between the absorption spectrum and the temperature. In this way the temperature is determined to be $48\pm2$ eV. The weak functional dependence of the transmission on density, which is uncertain to 20%, introduces only 1 eV of the total error. With the temperature accurate to better

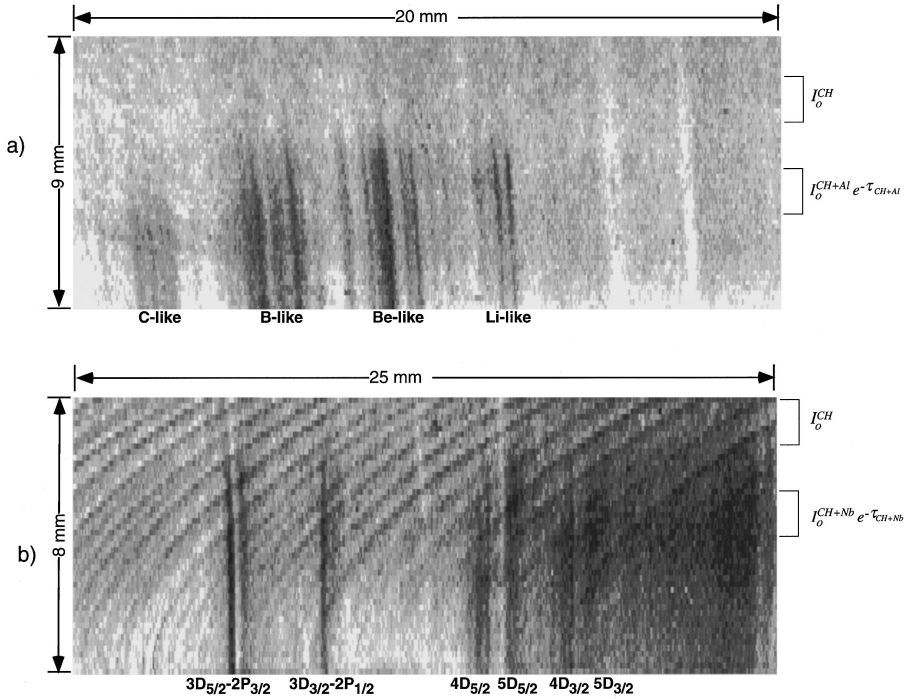


FIG. 9. Film data from spectrometer 1 used to measure the absorption spectra: (a) the aluminum spectrum and (b) the niobium spectrum. The diagonal curved lines in the niobium spectrum are from defects in the crystal. In both (a) and (b) the absorption spectrum is toward the bottom of the picture and the unattenuated backlight spectrum is at the top.

than $\pm 5\%$ and the density determined to 20%, it is possible to make quantitative comparisons between the experimental results for niobium and the theoretical calculations for the opacity.

## V. DISCUSSION OF OPACITY CALCULATIONS AND COMPARISON TO EXPERIMENT

The calculation of the opacity Eq. (5), which is used in modeling astrophysical and laboratory plasmas, requires three separate elements. First, there is the need to determine the atomic physics of the element of interest. Thus the level structure, the statistical weights, and the relevant matrix elements need to be determined. We note that, in particular, the dipole matrix elements are used to evaluate the absorption oscillator strength, but, equivalently, use can be made of the Einstein spontaneous radiative decay rate or other measures of the dipole strength. In Eq. (5) the spectral position of the absorbing transition $\nu$, the absorption strength, and the shape of the atomic cross section $\alpha$ are all part of the atomic physics relevant to the problem.

Second, the populations of the various states of the systems, i.e., the level populations in all the ion stages, are required. Thus the opacity calculations need the equation of state (EOS) or the ionization balance, which in the simplest LTE constructions could be a Saha-Boltzmann type model [12]. In Eq. (5), therefore, the EOS would provide the $n_j$.

The third and final element of the calculation of an opacity is the most difficult to isolate because a model is required that will be used to construct the opacity. Here the many assumptions and approximations are brought together to provide the calculational scheme by which the fundamental information, obtained from the atomic physics and the EOS, are turned into an opacity. There are several categories of

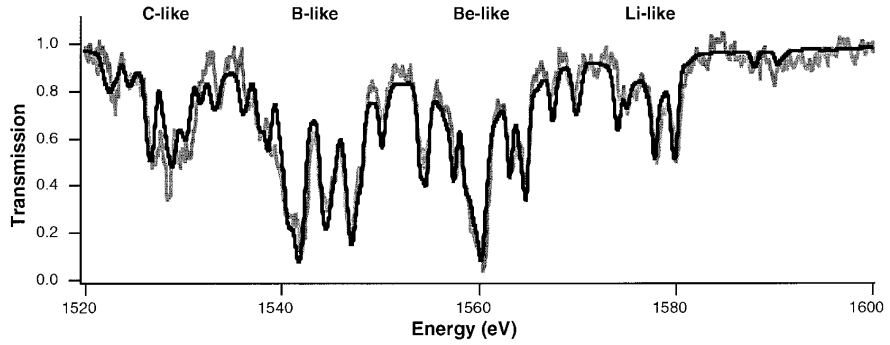


FIG. 10. Comparison of the absorption data with calculation shown as transmission versus energy in eV for the Al spectrum. The calculations are shown as solid lines, while the measurements are overlaid as gray lines. The aluminum spectrum was found to match the OPAL opacity code best at a temperature of 48 eV.

approximations. The most obvious place where an approximation scheme is required is the method by which the plasma effects are incorporated into the model. Thus, for example, the line profiles, which can be Stark broadened, and the continuum lowering, which limits the number of levels to be included, must be defined. Next, there are the simple calculational approximations required by the limitations of both human and computer time. For example, the number of levels that can be included in detail and the highest principal quantum number (PQN) included are usually restricted in some way. In addition, the manner in which the frequency dependence of the transition cross sections is included is one of the fundamental aspects of the opacity calculations. Of course, the line profiles may be Stark broadened; but, there is also the possibility, especially for complex configurations, that the transitions are best represented by an unresolved transition array (UTA) formalism, or as sums of UTAs as in the STA model discussed briefly below. In this manner, one implements a formulational model that provides the prescription for creating the opacity.

These three elements would, in a completely unified theory of opacity, be self-consistently determined. However, such a theoretical construct does not currently exist and is nowhere in sight. Therefore, we describe four different opacity calculations, each with a distinct theoretical basis, which will be compared to the experimental results. The comparison with the experimental data will demonstrate quite clearly that one does indeed require experimental results of the precision reported here to differentiate between the theoretical models.

The four calculations of opacity are HOPE [13], ENRICO [14], STA [15], and THERMOS [16]. The HOPE calculation performs the atomic physics using a self-consistent Dirac-Fock-like average atom (AA) model for the bound and continuum wave functions. Then the populations are formed by the assumption that Boltzmann statistics are valid. Next, since one has an average atom, the need to find the discrete ionization stage transition is achieved by using the AA wave functions and first-order perturbation theory to determine the correct energy from different configurations.

The ENRICO code developed by Albritton, Liberman, and Wilson computes the opacity in an extremely inventive manner by tracking a configuration history of a test ion in an ambient plasma. An arbitrary $J$-$J$ coupled configuration is chosen and then the rates for each radiative decay process by which the configuration can change are calculated. A configuration is chosen randomly, with the selection process biased by the magnitude of the rates. It can be shown that the configuration space is properly sampled by including only one process, e.g., radiative ionization, and its inverse process. The energies of the states are calculated by the solution of the Dirac equation in a self-consistent field using a local-density approximation for the exchange-correlation functional. The bound-bound absorption cross section is treated in an UTA approximation with only dipole radiative oscillator strengths considered.

The STA calculation employs an accurate fully relativistic and quantum-mechanical theory using the parametric potential approach including configuration interaction between neighboring $J$-$J$ configurations. Plasma effects are taken into account using a consistent average potential calculated in the ion sphere model, yielding continuum lowering and the chemical potential, which together with Boltzmann statistics provides the level populations. The profiles of individual lines are calculated as Voigt functions, with Doppler broadening providing the Gaussian width and electron collisional broadening providing the Lorentzian width. This method is capable of making the transition between detailed line accounting methods and the detailed configuration accounting (UTA) method.

TABLE I. Comparison of global parameters for the four opacity calculations of an Al-Nb mixture with $\rho=2.6\times10^{-2}$ g/cm$^3$ and a temperature of 47 eV.

| Code | $Z^*$ for Al-Nb | $\kappa_R$ ($10^3$) | $\kappa_P$ ($10^3$) |
|---|---|---|---|
| HOPE | 10.16 | 4.23 | 8.50 |
| ENRICO | 10.30 | 4.60 | 9.09 |
| STA | 10.39 | 4.66 | 9.31 |
| THERMOS | 11.11 | 5.59 | 9.61 |

Finally, the THERMOS calculation uses a self-consistent field model with the Dirac equation for the orbitals with the PQN less than or equal to 3, with the Pauli approximation to the Dirac equation for the PQN greater than 3. The atomic physics is achieved in an average atom approximation and then perturbation theory is used to calculate the energy levels of the different configurations. The populations are provided by a Gibbs-type formula. In those cases where there is a large number of configurations the UTA method is applied, while for the individual transitions line shapes, Voigt functions are used with the Lorentzian widths given by the sum of the electron and natural broadening, while the Gaussian width is given by the Doppler effect.

Using these opacity codes, calculations have been performed for the conditions determined in the experiment discussed in Sec. IV, i.e., $\rho=2.6\times10^{-2}$ g/cm$^3$ and $T_e=47$ eV. A comparison of the various results can be discussed using various global aspects of the calculated opacities. First, the mean charge state $Z^*$, defined as $\Sigma n_i Z_i/\Sigma n_i$, provides a measure of the ionization balance and therefore a measure of the calculations of the populations. Second, the Rosseland mean opacity $\kappa_R$ [17], a harmonic mean, defined by

$$\frac{1}{\kappa_R}=\int d\nu\,\frac{1}{\kappa_\nu}\frac{\partial B_\nu}{\partial T}\Bigg/\int d\nu\,\frac{\partial B_\nu}{\partial T},$$

is both useful in the calculation of the radiation energy flow in various plasma simulations [18] and provides insight into the nature of the low opacity contributions, i.e., the so-called windows, in the spectral range $h\nu\sim3.8kT$. Finally, the Planck mean opacity $\kappa_P$, a standard mean defined by

$$\kappa_P=\int d\nu\;\kappa_\nu\Bigg/\int d\nu,$$

favors large oscillator strength transitions and can be an important test of the conservation of the oscillator strength. Table I represents the various values derived from the four calculations.

In Table I the ionization balance for the mixture $Z^*$ can be seen to be similar in the first three cases with the result

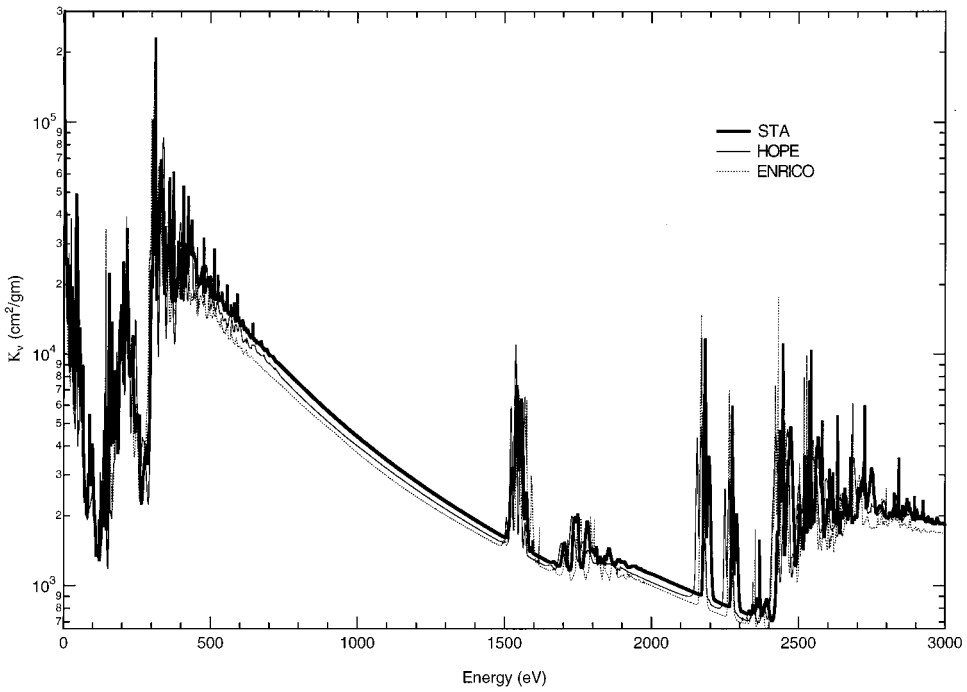


FIG. 11. Calculated opacity in cm$^2$/gm or the Al-Nb mixture versus energy in eV for the three codes HOPE, ENRICO, and STA. The results of STA are presented as a thick line, those of HOPE are a thin line, and the ENRICO results are given by a dotted line. The experiment covers both the Al *K*-shell spectrum in the 1500–1600 eV region (see Fig. 10) and the Nb spectrum from 2100 to 2800 eV (see Fig. 13).

from THERMOS being distinct. We note that a change of unity in the $Z^*$ implies that a shift in the spectrum by an entire ion stage would be observable. To simplify further comparisons, therefore, we point out that either THERMOS *or* the other codes are correct for this case and, as it turns out, the latter is true. We will see from the analysis below that HOPE, ENRICO, and STA have the broadly correct spectral character. Thus we can remove THERMOS from the spectral comparisons.

The $\kappa_R$ values, which strongly weight the windows, i.e., the low opacity values, in the spectral regions around 180 eV have similar values for HOPE, ENRICO, and STA. In addition, there is a large value for the THERMOS code due to its implementation of the UTA model to broaden the transition arrays, thus filling in the low opacity contributions. Finally, the fact that the $\kappa_P$ values are quite similar indicates that the various codes have about the same total oscillator strength. The lower value for the HOPE code is due to the cutoff on the high PQN implemented.

In Fig. 11 we show the opacities of the three relevant cases, eliminating THERMOS, which has a poor ionization balance, to make the figure more illustrative. The figure represents the opacities $\kappa_\nu$ for the three cases versus the energy in eV, showing that the dominant features are in three spectral regions. In the low-energy range (0–0.5 keV) the features are due to a combination of Al and Nb, in the mid-energy range (1.5–2.0 keV) the features are due to the Al *K* shell, and in the high-energy range (2.1–2.8 keV) they are due to the Nb *L* shell. The high-energy spectral range covers the region measured in the experiment. Figure 11 shows that generally the three opacity calculations reproduce the same gross structures. However, to differentiate between the various calculations in order to ascertain which approach provides accurate opacities requires a more detailed view. The results of the experimental observation of the Nb emphasize the spectral region from 2.1 to 2.8 keV, where the transmission is measured; see Eqs. (2) and (8).

For the measured plasma conditions and spectral range we show the transmission versus energy predicted by the HOPE, ENRICO, and STA calculations in Fig. 12. The transmission has been convolved with an instrument function that is 1 eV wide to show the observable transmission. Note that this changes the theoretical spectra little as there are few features with small intrinsic widths. Figure 12 clearly shows that comparison of spectra with this level of detail, given the deviations seen in the figure, will be complex. To simplify we represent the STA result, which we determine below (see Fig. 14) to provide the best agreement to data, as the thick line. The HOPE result is shown as a thin line and the ENRICO result is shown as a dotted line. The figure is also labeled with the configurations that contribute to the opacity in the various spectral regions. It is obvious, however, that the position and shape of the spectra are quite distinct.

There are two possible reasons for the relative shift of similar features in the three calculations. First, the difficulties of calculating precise transition energies can lead to relative shifting of the spectrum. In this way, taking as an example the $3D_{5/2}$-$2P_{3/2}$ features at $\sim$2180 eV, one can see that an accuracy of better than 0.25% in the energy would be required to discount the atomic physics as a source of the shift of this feature. In individual calculations of particular transition energies, this level of accuracy can be attained; however, in opacity calculations where upward of $10^5$ transitions are needed, compromises are often necessary. For a more general discussion of accuracies in the calculation of atomic energy levels see Cowan's comments [19].

Second, the spectral features are not made up of single

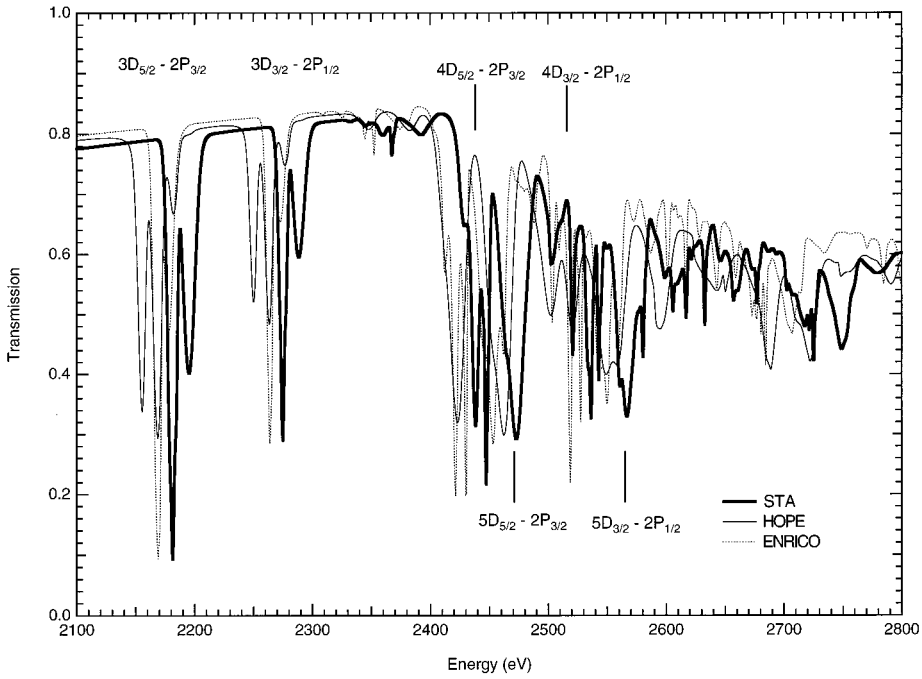


FIG. 12. Details of the calculations represented as transmission versus energy in eV for the three calculations represented in Fig. 11. The various configurations are also labeled. The complexity of the spectrum is apparent from the figure.

transitions, but are an amalgam of similar transitions from numerous ionization stages. In fact, the number of transitions in a feature can be so large that statistical treatments provide a method of determining the spectral feature characteristics. For example, see the discussions of unresolved transition arrays by Bauche *et al.* [20].

We can now discuss the present calculations more specifically. First, the calculations of the energy levels in the spectral range of interest here is even more demanding than one might at first suspect as the energy range of interest is much larger than the thermal energy. This indicates that the importance of the atomic physics calculations will be enhanced and in the present case great care is needed to obtain the transition energies including orbital relaxation, as in the STA calculation. Thus the wave functions for the excited as well as the ground states of each transition must be calculated in detail. Second, we note that the ionization balance will play a role; we show in Fig. 13 the ionization fraction versus niobium charge state for the three opacity calculations. Here we see that ionization balance of all the calculations is peaked near charge state 12; however, the mean Nb charge state is 11.37, 11.75, and 12.15 for the HOPE, STA, and ENRICO calculations, respectively. Further, the effect of the ionization balance can be seen clearly in the $2p$-$3d$ transition arrays where one can easily distinguish between transitions that arise from Nb ions with 17 electrons in the $n=3$ shell and end with 18 electrons and those that start with 16 and end with 17. Thus the HOPE calculations show, in the $2p$-$3d$ arrays at energies of $\sim$2180 and $\sim$2280, the ionization balance differences. This is in keeping with the results in Fig. 13. We also note that the transition from the lower ionization stages should be shifted to lower energy and here we see that the HOPE calculations are to the low-energy side of those of either ENRICO or STA.

Above, we examined the effect on the $2p$-$3d$ transition energy due to the addition of an electron in the $3d$ shell and found that the effect is observable. However, the effects of the screening of the added electron will differ depending on the final-stage shell of the transition, assuming that we are always looking at $2p$ absorptions, and also which shell receives the extra electron. In Table II we show the values for the shift in transitions energies due to the addition of an $n=3$ or 4 electron.

In Table II we see that the shift of the $2p$-$3d$ of 18 eV due to an $n=3$ electron is in fact the source of the two peaks in the $2p$-$3d$ absorption feature. We also note that the ENRICO opacity has broadly the same ionization balance, as witnessed both by Fig. 13 and by the relative absorption of

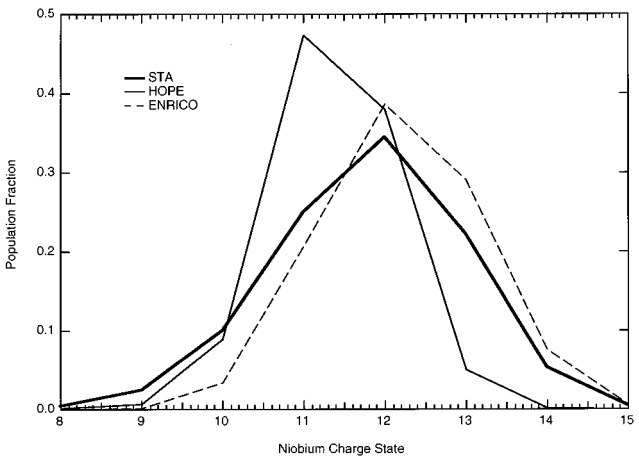


FIG. 13. Ionization fraction versus the charge state for Nb at a temperature of 47 eV and a density of 0.26 g/cm$^3$ for the three opacity calculations: STA, thick solid line; HOPE, thin solid line; and ENRICO, dashed line. The ion fractions are represented as continuous curves for clarity.

TABLE II. Shift in energy in eV of various transitions caused by adding one electron to either the $n=3$ or 4 level of Nb XII.

| Transition | Shift (eV) for added $n=3$ electron | Shift (eV) for added $n=4$ electron |
|---|---|---|
| $2p$-$3d$ | 18 | 0–1 |
| $2p$-$4d$ | 35 | 5–7 |
| $2p$-$5d$ | 45 | 8–10 |
| $2p$-$6d$ | 50 | 12–13 |

the $2p$-$3d$ features, but the transitions lie towards lower energy. This implies that the calculations of the atomic physics gives rise to the differences between the STA and ENRICO opacities.

This analysis allows us to isolate the remainder of the disagreement to the atomic physics calculations. It is at this juncture that the need for experimental data becomes abundantly clear. Thus, to resolve this issue we show in Fig. 14 the niobium transmission calculated using the STA method [12], compared to the experimental transmission data. Here we have again introduced an instrumental profile width of 1 eV for comparison. In general, the agreement between theory and experiment is excellent. However, there are some regions of the spectrum where there are some differences, most notably the shape of the $5D_{5/2}$-$2P_{3/2}$ features. Further, given the comparison of the different opacity results in Fig. 12, one can easily understand that the STA model provides the only reasonable fit to the data. This, in turn, indicates that it is essential to include both a good model for the EOS and the orbital relaxation in the atomic physics calculations to obtain good agreement.

Thus the purpose here, i.e., to examine techniques for extracting quantitative data, has been shown to be successful, noting that the principles laid out in Sec. II are satisfied in the experiment presented here. The use of the simulations was critical in achieving an understanding of the criteria for designing the target, but were not invoked to derive data. These data then permit us to differentiate among the various competing theories, finding a correct calculation from the four possibilities.

## VI. DISCUSSION OF ABSORPTION EXPERIMENTS

Various applications of the techniques presented in Sec. II are discussed in this section. To illustrate the difficulties involved we compare three separate experiments that attempt to extract information from an absorption experiment.

The three examples use different techniques to achieve similar goals. The first is the point projection backlighting technique (PPS) described in detail in Balmer *et al.* [22], used by Perry *et al.* [1] for the measurement of the x-ray transmission of an aluminum sample and extended in the present work. The second is the measurement by Da Silva *et al.* [3] of the iron transmission using a large area backlight source and a streak camera coupled to a grating to obtain data in the soft-x-ray range. For convenience we refer to this as the soft-x-ray streak camera (SXSC) method. Finally, Bruneau *et al.* [4] used a large area backlight to measure the absorption spectrum in the x-ray region to study a germanium sample. For convenience we refer to this method as the backlight and static spectrometer (BLSS) method. In each of the experiments the method to obtain the required quantities is different and their application provides a way to define the bounds of the experimental technique.

We touch on the following aspects of the experiments: extraneous sources of signal: film fog, fluorescence, and background emission (Sec. VI A) measurement of the backlight (Sec. VI B); measurement of the absorption (Sec. VI C); and the analysis of the data, that is, the reduction of the raw film data to the desired physical quantity (Sec. VI D). For each of these areas we will contrast the experimental approaches. More importantly, we will show at each step in the analysis where problems arise.

### A. Extraneous signals

In the three methods the information on the extraneous signals was obtained differently. In the PPS method the background signals are all available on the film record. The emission can be extracted from signals on the outside of the frame that is formed by the projected image of the point source backlight. Film fog and fluorescence is also available on the borders of the film that are blocked from the source of light. In this way the various contributions can be determined. In the PPS method the primary difficulty is that the emission is un-imaged and therefore one must assume that the emission contribution that falls in the frame can be interpolated from information taken from the edges. Further, when temporal resolution is provided by the duration of the backlight then the emission is time integrated. This latter

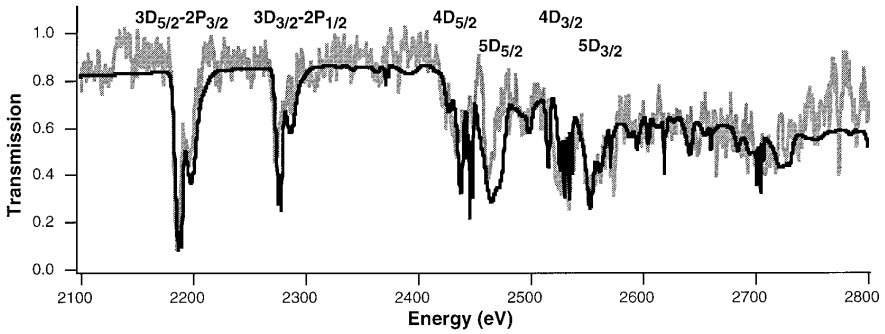


FIG. 14. Comparison of the absorption data with calculation shown as transmission versus energy in eV for the Nb spectrum. The calculations are shown as solid lines, while the measurements are overlaid as gray lines. The STA model was used to calculate the niobium opacity at the temperature and density determined by the experiment.

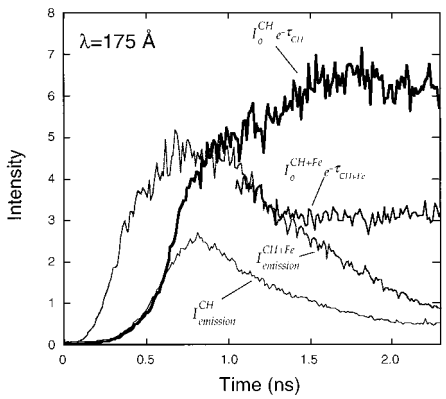


FIG. 15. Four results taken from the experiments of Da Silva *et al.* The four recorded intensities are shown as a function of time. The wavelength at which the time histories are taken is 175 Å. The four signals correspond to the four measurements necessary to solve Eq. (9) for the transmission. In the experiment the heating pulse starts at $t=0$ and ends at $t=1.1$ ns. The backlight is delayed by 0.5 ns. Note the slight increase in signal of $I_0^{\mathrm{CH+Fe}}e^{-\tau_{\mathrm{CH+Fe}}}$ at late times.

problem can be obviated by using a gated x-ray camera [23]. Alternatively, it is possible to show in some cases that the emission is negligible [24].

The SXSC method used a space-integrating instrument and therefore the experiment was performed in four separate steps, with each one obtaining one piece of the data as indicated in Eq. (9). The observation of the various components of the signal for the Da Silva *et al.* experiment are shown in Fig. 15. To obtain the soft-x-ray spectrum around 175 Å in a relatively low-temperature plasma, a single Au burnthrough foil lasting 1 ns was the x-ray-heat source, and therefore the backlight, also a Au burnthrough foil but delayed in time and distance, would cause some observable heating of the sample. In Fig. 15 the late-time behavior of the sample shows emission when backlight alone is employed. The relative amplitude of this backlight is weak, being a factor of 15% below that of the absorption source; however, without temporal resolution it would be difficult to extract this emission from the film record.

In the BLSS method two spectrometers are used: one to measure the absorption spectrum and a second to measure the backlight spectrum. There is no independent measurement of either the emission or the fluorescence, making quantitative analysis difficult. For example, large optical depths, which translate into low signal levels, can be especially troublesome: a 0.1 optical density difference in the base-line correction of the film can lead to errors of 25% in the results for optical film densities on SB2 film in the range 0.2–2.0 [25]. If the reference spectrum is not from the same laser shot, then laser energy fluctuations, target variations, and target focusing will increase the error of the measurement. Of course, to ensure that the data are in a region of the film density versus exposure curve that has a small gradient eases this problem considerably.

### B. Measurement of the backlight

In PPS the absorption and backlight spectra are recorded simultaneously. In this way the measurement of the $I_{\mathrm{film}}^{\mathrm{CH}}$ of Eq. (6) can be obtained. There remains the need to prove that the emission from the CH tamper does not contribute and this can be performed on a separate experiment. Note that the emissivity is low in the PPS case due to the fact that the region we are probing is greater than 1500 eV, while the sample temperature is ~50 eV. On the other hand, for measurements in the soft-x-ray region emission contributions to the film record must be minimized. In the case of Springer *et al.* [23], where spectra in the region of 100 eV was measured, gating of the spectrometer achieved the desired result by minimizing the exposure of the film to the duration of the backlight.

A further problem that arises with PPS is that, although the method is two dimensional, in the dispersion dimension the spatial information is convolved with spectral information. Thus, if gradients occur along the dispersion direction, i.e., the $r$ direction in Fig. 2, different parts of the spectrum may arise from regions with somewhat different optical paths.

For SXSC the solution is to perform separate measurements and, as with sources of emission, this is dependent on the reproducibility of the backlight source. The problem of spatial uniformity is addressed in this approach by using a slit in the direction perpendicular to the direction of the streak motion. This, however, does not allow one to obtain spatial information in the direction along the slit. Thus the non-uniformity of the sample in size, temperature, and density cannot be removed. To offset any gross non-uniformity the SXSC method should employ a number of imaging diagnostics to measure the uniformity of emission. These instruments would provide *indirect* information on sample uniformity.

In BLSS the backlight spectrum was measured with a separate spectrometer. The spectrum was then used to determine $I_0$ and subsequently was used in the determination of the transmission. This is an improvement over the separate experiment method of SXSC since it allows the measurement of the backlight on the same experiment as the absorption measurement. However, the need to compare data from two spectrometers on an absolute basis is less ideal than the PPS method. In addition, any lack of spatial uniformity would be hidden by the space integration of the spectrometers.

The need for two spectrometers can be avoided by using a sample that is split, in a manner similar to that used by Bauer *et al.* [24] There the spectrometer, by use of a slit, has spatial resolution in one direction. Thus the spectrum due to the backlight and the backlight attenuated by the sample can be measured.

### C. Measurement of the transmission spectrum

The recording of the transmission spectrum as indicated in Eq. (9) is, of course, the goal of the experiments. However, as indicated in Eq. (9), the data recorded do not simply relate to a single plasma condition unless care is taken to ensure the sample is uniform in both temperature and density, as discussed in Sec. III. To ensure that the transmission measurement can be reduced to a study of the absorption coefficient [see Eqs. (3)–(5)] tests on the samples of interest should be performed. In some cases, where the behavior of

the tamping material itself was of interest [24,26] or only gross absorption features are of concern [3], one can relax the need for sample uniformity in the direction along the line of sight.

The differences in the density along the line of sight have been addressed in only one experiment and then only indirectly. Perry *et al.* [27] measured the absorption of the same target but with two different thicknesses, one three times the other. This provides indirect information on the transverse gradient, since the transmission through the two thicknesses would amplify any density gradients, but no measurable differences were found.

One difficulty for all techniques is the instrument response function that broadens the spectrum. In the case of an emission spectrum the strong signal regions are smoothed but remain strong. In absorption, however, the instrumental smoothing could give false absorption information. For example, for transmission data that are accurate to 3%, it is impossible to distinguish between an optical depth of 3.5 or *any* greater value. Further, small extraneous signals that fill in these regions of high absorption could also seriously affect the interpretation.

### D. Reduction of the data

In the PPS method the reduction of the data using Eq. (8) is straightforward insofar as all the information including the extraneous signals is available. Thus, if the material is uniform with a known path length we can reduce the data to the transmission of the sample.

In the SXSC case the goal was to verify the existence of a gross spectral feature predicted by a new theoretical model. In this case we therefore must ensure that all the measurements are sufficient to provide qualitatively accurate data. As shown in Fig. 11, the signals from the four components of the experiment were obtained on separate experiments maximizing errors from shot to shot variations in laser performance, target reproducibility, and procedural problems, such as target alignment. However, the reproducibility was deemed sufficient for the purpose of the experiment.

In the BLSS case the data reduction was intended to obtain the ionization state distribution and from this the temperature. This is a far more difficult experiment to analyze, since there is no independent verification of the primary plasma conditions and no independent verification of the theoretical optical depth model. We note that a similar temperature and density regime was studied for Ge and a reasonable representation for the transmission was provided by the STA model [21,27]. However, the STA model predicts large opacity for the temperature, density, and sample conditions provided by Bruneau *et al.* [4]

In the analysis of the BLSS data the areal density is used as a free parameter to bring the measured optical depth into agreement with the theoretical opacity model. Use of the initial areal density gives an optical depth larger than 4 in the single broad spectral feature used in the subsequent analysis. Thus the extracted data, i.e., the transmission and eventually the optical depth, would have large associated errors due to the relative weakness of the signal. A discussion of the difficulties entailed in using the derived optical depth in lieu of the transmission data is presented by Perry *et al.* [27]

The two-dimensional analysis above indicates that at *worst*, mean areal density drops by a factor of 20% at 3 ns if the entire sample is probed; but this is not consistent with the analysis of the BLSS data. On the one hand, if the sample had radial gradients the low areal density regions would transmit the backlight source and cause a filling in of the absorption features. This would act as an extraneous signal on film and would compromise the absorption measurement. On the other hand, if there were no, or small, radial gradients involved in the measurement, due to restricting the field of view to the central region of the sample, there could be little justification for the assumption of the mass loss.

That there was a consistency found between the opacity model employed and the optical depth obtained by data reduction is attributable to the analysis method, which had enough adjustable parameters to ensure this. That is, the iterative system is unconstrained by the physical parameters that are to be determined in the iterative process. Thus the determination of the average ionization state $Z$ and from this the temperature, which is dependent on the validity of the opacity model and the assumed loss of mass, are suspect.

## VII. SUMMARY

The PPS absorption technique discussed here provides a method to characterize quantitatively the state of a hot, dense plasma. When this is coupled to experimental designs that provide plasma samples with minimized temperature and density gradients the technique becomes very powerful. Absorption measurements can provide a diagnostic of the ionization state and the ion and the electron densities, as well as the temperature. In the experiment reported here, sample density and temperature were obtained simultaneously with the transmission measurement. The independent density measurement together with the inferred temperature provide sufficient characterization of the sample to allow for a quantitative comparison between experiment and theoretical models of the niobium transmission spectrum. Given the difficulty in obtaining quantitative data for hot, dense matter, this is a much needed technique for data generation.

The requirements to obtain meaningful quantitative data using this technique were discussed in detail. We have shown in simulations that the tamped targets act to hydrodynamically constrain the enclosed sample material. The samples then have small density and temperature gradients along the line of sight for regions near the center of irradiation symmetry. However, the two-dimensional simulations indicate that spatially unresolved measurements of the absorption spectrum can suffer severely from lateral transport. In fact, the case is clear that complete tamping and restriction of the observation to the region near the symmetry axis is advisable. A review of two previous experiments that utilized absorption spectroscopy [3,4] was given as examples of experiments with similar goals, but indicated that serious problems can arise in the data analysis when compromises are made in the experimental design.

[1] T. S. Perry *et al.*, Phys. Rev. Lett. **67**, 3784 (1992); J. Edwards, V. Barrow, O. Willi, and S. J. Rose, Europhys. Lett. **11**, 631 (1991); P. Springer *et al.*, Phys. Rev. Lett. **69**, 3735 (1992); B. A. Hammel *et al.*, in *Proceedings of the 1991 Radiative Properties of Hot Dense Matter Workshop*, edited by W. H. Goldstein, C. F. Hooper, J.-C. Gauthier, J. R. Seely, and R. W. Lee (World Scientific, Singapore, 1991), p. 22

[2] S. J. Davidson, J. M. Foster, C. C. Smith, K. A. Warburton, and S. J. Rose, Appl. Phys. Lett. **52**, 847 (1988); J. M. Foster *et al.*, Phys. Rev. Lett. **67**, 3255 (1991).

[3] L. Da Silva *et al.*, Phys. Rev. Lett. **69**, 438 (1992).

[4] J. Bruneau, A. Decoster, D. Desenne, H. Dumont, J.-P. Breton, M. Boivineau, J.-P. Perrine, S. Bayle, M. Louis-Jacquet, J.-P. Geindre, C. Chenais-Popovics, and J.-C. Gauthier, Phys. Rev. A **44**, R832 (1991).

[5] J. Balmer, C. L. S. Lewis, R. E. Corbett, E. Robertson, S. Sadaat, D. O'Neill, J. D. Kilkenny, C. A. Back, and R. W. Lee, Phys. Rev. A **40**, 330 (1989); D. M. O'Neill, C. L. S. Lewis, D. Neely, S. J. Davidson, S. J. Rose, and R. W. Lee, *ibid*. **44**, 2641 (1991); J. Koch *et al.*, J. Quant. Spectrosc. Radiat. Transfer **54**, 227 (1995); S. Gary *et al.*, *ibid*. **54**, 155 (1995).

[6] See, for example, D. Mihalas, *Stellar Atmospheres* (Freeman, San Francisco, 1978).

[7] D. R. Kania *et al.*, Phys. Rev. A **46**, 7853 (1992); C. A. Back *et al.*, J. Quant. Spectrosc. Radiat. Transfer **51**, 19 (1994).

[8] G. B. Zimmerman and W. L. Kruer, Comments Plasma Phys. **2**, 51 (1975).

[9] C. L. S. Lewis and J. C. McGlinchey, Opt. Commun. **53**, 179 (1985); J. M. Foster, Rev. Sci. Instrum. **59**, 1849 (1988).

[10] F. J. Rogers and C. A. Iglesias, Astrophys. J. Suppl. **79**, 507 (1992).

[11] C. A. Iglesias, J. K. Nash, M. H. Chen, and F. J. Rogers, J. Quant. Spectrosc. Radiat. Transfer **51**, 125 (1994); see also J. Abdallah and R. E. H. Clark, J. Appl. Phys. **69**, 23 (1991).

[12] D. Mihalas, *Stellar Atmospheres* (Ref. [6]), p. 108.

[13] B. F. Rozsynai, Phys. Rev. **145**, 1137 (1972); B. F. Rozsynai and M. Lamoureux, J. Quant. Spectrosc. Radiat. Transfer **43**, 381 (1990); A. Goldberg, B. F. Rozsynai, and P. Thompson, Phys. Rev. A **34**, 421 (1986).

[14] B. Wilson, J. Albritton, and D. Liberman, in *Radiative Properties of Hot Dense Matter*, edited by W. H. Goldstein, C. F. Hooper, J.-C. Gauthier, J. R. Seely, and R. W. Lee (World Scientific, Singapore, 1991), and references therein.

[15] A. Bar-Shalom *et al.*, Phys. Rev. A **40**, 3183 (1983).

[16] A. F. Nikiforov *et al.*, Vopr. At. Nauk. Teck. **4**, 16 (1976); V. G. Novikov *et al.*, Teplofiz. Vys. Temp. **31**, 881 (1993).

[17] D. Mihalas, *Stellar Atmospheres* (Ref. [6]).

[18] For a discussion of relevant opacity approximations see F. J. Rogers and C. A. Iglesias, Science **263**, 50 (1994).

[19] R. D. Cowan, *The Theory of Atomic Structure and Spectra* (University of California Press, Berkeley, 1981).

[20] J. Bauche, C. Bauche-Arnoult, A. Bachelier, and W. H. Goldstein, J. Quant. Spectrosc. Radiat. Transfer **54**, 43 (1995), and references therein.

[21] A. Bar-Shalom, J. Oreg, and W. H. Goldstein, in *Radiative Properties of Hot Dense Matter* (Ref. [14]).

[22] See the paper by Balmer *et al.* in Ref. [5] and references therein.

[23] P. T. Springer *et al.*, J. Quant. Spectrosc. Radiat. Transfer **51**, 371 (1994).

[24] J. D. Bauer *et al.*, Phys. Rev. E **52**, 6736 (1995).

[25] B. L. Henke, F. G. Fujiwara, M. A. Tester, C. H. Dittmore, and M. A. Palmer, J. Opt. Soc. Am. B **1**, 828 (1984).

[26] B. A. Hammel *et al.*, Europhys. Lett. **20**, 319 (1992); J. Seely *et al.*, J. Quant. Spectrosc. Radiat. Transfer **51**, 349 (1994).

[27] T. S. Perry, K. S. Budil, R. Cauble, R. A. Ward, D. R. Bach, C. A. Iglesias, B. G. Wilson, J. K. Nash, C. C. Smith, J. M. Foster, S. J. Davidson, F. J. D. Serduke, J. D. Kilkenny, and R. W. Lee, J. Quant. Spectrosc. Radiat. Transfer **54**, 317 (1995).